INTERFACE

royalsocietypublishing.org/journal/rsif

Research

Cite this article: Kadry K, Olender ML, Marlevi D, Edelman ER, Nezami FR. 2021 A platform for high-fidelity patient-specific structural modelling of atherosclerotic arteries: from intravascular imaging to three-dimensional stress distributions. *J. R. Soc. Interface* **18**: 20210436.
https://doi.org/10.1098/rsif.2021.0436

Received: 26 May 2021
Accepted: 2 September 2021

Subject Category:
Life Sciences–Engineering interface

Subject Areas:
computational biology, biomechanics, biomedical engineering

Keywords:
intravascular imaging, structural mechanics, coronary atherosclerosis, personalized medicine, multi-material models, three-dimensional reconstruction

Author for correspondence:
Karim Kadry
e-mail: kkadry@mit.edu

A platform for high-fidelity patient-specific structural modelling of atherosclerotic arteries: from intravascular imaging to three-dimensional stress distributions

Karim Kadry[1,2], Max L. Olender[1], David Marlevi[1], Elazer R. Edelman[1,3] and Farhad R. Nezami[4]

[1]Institute for Medical Engineering and Science, Massachusetts Institute of Technology, Cambridge, MA, USA
[2]Laboratory of Hemodynamics and Cardiovascular Technology, Swiss Federal Institute of Technology, MED 3.2922, 1015 Lausanne, Switzerland
[3]Cardiovascular Division, and [4]Thoracic and Cardiac Surgery Division, Brigham and Women's Hospital, Harvard Medical School, Boston, MA, USA

KK, 0000-0001-9520-0504; MLO, 0000-0002-0936-5300; FRN, 0000-0002-4210-3177

The pathophysiology of atherosclerotic lesions, including plaque rupture triggered by mechanical failure of the vessel wall, depends directly on the plaque morphology-modulated mechanical response. The complex interplay between lesion morphology and structural behaviour can be studied with high-fidelity computational modelling. However, construction of three-dimensional (3D) and heterogeneous models is challenging, with most previous work focusing on two-dimensional geometries or on single-material lesion compositions. Addressing these limitations, we here present a semi-automatic computational platform, leveraging clinical optical coherence tomography images to effectively reconstruct a 3D patient-specific multi-material model of atherosclerotic plaques, for which the mechanical response is obtained by structural finite-element simulations. To demonstrate the importance of including multi-material plaque components when recovering the mechanical response, a computational case study was conducted in which systematic variation of the intraplaque lipid and calcium was performed. The study demonstrated that the inclusion of various tissue components greatly affected the lesion mechanical response, illustrating the importance of multi-material formulations. This platform accordingly provides a viable foundation for studying how plaque micro-morphology affects plaque mechanical response, allowing for patient-specific assessments and extension into clinically relevant patient cohorts.

1. Introduction

Characterization of arterial structures such as atherosclerotic plaques is critical for diagnosing and tracking cardiovascular disease. Disruption of these structures accounts for many pathologies such myocardial infarction, stroke and peripheral vascular disease. Myocardial infarction in particular is a potentially fatal clinical complication, which induces irreversible damage to the myocardium due to obstructed blood supply through the coronary arteries. Multiple studies have shown that internal plaque morphological markers, such as a large lipid core and thin fibrous cap, along with a high plaque burden improves the identification of the so-called *vulnerable*, rupture-prone plaques [1–3], providing insights into both stability and remodelling mechanisms. Yet, a distinct portion of these phenotypes do not experience rupture [1,4], highlighting the need for improved risk stratification for lesion vulnerability and rupture prediction. To address this, the assessment of lesion mechanical behaviour has been proposed as central in

THE ROYAL SOCIETY PUBLISHING

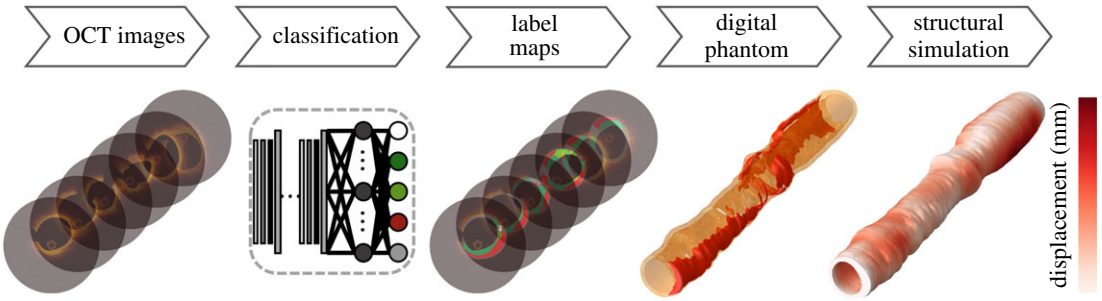

Figure 1. An overview of the computational platform. Starting from a series of OCT images, the vessel borders are delineated through a mechanics-based surface-fitting technique. The pixels within the vessel wall are classified into different tissue types with a convolutional neural network to produce segmented label maps. The label maps are then converted into a 3D multi-material mesh, which is used as the basis for structural mechanics simulations to calculate high-fidelity displacement and stress fields for the lesion.

understanding plaque stability. Computational finite-element (FE) modelling is a promising tool that can provide much needed insight into local mechanical lesion behaviour. Early two-dimensional (2D) FE studies indicated a correlation between high plaque structural stress (PSS) and plaque rupture [5], as well as important vascular factors relating to decreased plaque stability, such as collagen degradation [6] and sustained inflammation [7]. Accordingly, there is increasing interest in the use of patient-specific *in vivo*-based models to further improve our understanding of clinical plaque behaviour and enhance current risk stratification protocols [8–10].

To facilitate the creation of such individualized *in vivo* models, advances in intravascular imaging have become central in providing input information on anatomy and intraplaque tissue composition. Intravascular ultrasound (IVUS) has been extensively used in 2D FE modelling studies, for both assessing lesion morphology and calculating PSS to identify vulnerable plaques and predict rupture location [11–13]. The simplifications imposed by 2D configurations, however, tend to overestimate intraplaque stresses compared with equivalent 3D models [14–16]. Such 2D models also cannot convey information about longitudinal plaque heterogeneity, a component recently proposed as critical in modulating plaque stability [17]. Moreover, IVUS-based models suffer from comparably limited image resolution, where an in-frame pixel size of around 200 µm impedes the reconstruction of potentially critical plaque structures, such as the thin fibrous cap separating a mural lipid pool from the luminal space. Specifically fibrous cap thickness has been understood to play a significant role in modulating PSS, with an exponential stress increase indicated with decreasing cap thickness [18,19]. The widely discussed thin-cap fibroatheroma (TCFA) lesion phenotype is also characterized by a cap thickness of less than 65 µm [20], again highlighting the limitations of IVUS-based computational plaque analysis.

Addressing the resolution limits of current IVUS systems, optical coherence tomography (OCT) is an alternative imaging modality providing in-plane resolutions of less than 20 µm. OCT-derived morphologies have been used to build 2D structural models of TCFA-like lesions [21,22], and recent attempts have striven to use OCT data to construct patient-specific 3D models of atherosclerotic lesions. Wang *et al.* [23] created a linear elastic fluid–structure interaction (FSI) model of a single lipid plaque component within a coronary artery using manually segmented OCT images; however, the difficulty in delineating the outer adventitial border of the lesion was highlighted as a particular hindrance. Owing to the pronounced signal attenuation at increasing penetration depth, an improper delineation of the vessel components can modify the resulting geometry, potentially influencing the estimation of derived PSS [21]. To rectify this issue, Guo *et al.* [24,25] proposed a hybrid IVUS-OCT approach in which IVUS images were used to manually reconstruct the inner and outer borders of the lesion, with data subsequently co-registered to the higher resolution OCT data from which intraplaque information was extracted. Although sophisticated, such a hybrid multi-modality approach requires multiple acquisitions, both being beyond standard clinical practice and introducing the need to precisely align images through co-registration and warping to account for spatial, physiological and resolution variations between different modalities and acquisitions.

Addressing the limitations of existing approaches, this work builds upon advances in 3D arterial modelling by leveraging several novel image-processing tools to generate patient-specific multi-material structural models of atherosclerotic plaques from a series of OCT images. To demonstrate the utility and efficacy of this platform, a coronary lesion from a clinical case was generated and used as the basis for a structural simulation. Furthermore, to highlight the importance of multi-material modelling, various virtual models of the same lesion were formulated in which the lipidic and calcific tissues were systematically included or excluded. To the best of our knowledge, this platform is one of the first to allow for such 3D multi-material modelling using clinically acquired OCT images as sole input, with plaque mechanical response being quantified in a semi-automated fashion. Accordingly, this platform represents a viable and novel tool with which to analyse detailed patient-specific mechanical behaviour of atherosclerotic lesions, being of value not only for improved insight into atherosclerotic risk stratification and clinical decision making but also for understanding fundamental mechanical lesion behaviour.

2. Methods

2.1. Methodological framework

The computational platform presented here transforms a series of OCT images into a patient-specific, multi-material structural model of an atherosclerotic lesion for structural simulation (figure 1). This section provides methodological details for this platform, which includes image-based tissue characterization, 3D model generation and discrete numerical configuration.

2.1.1. Tissue label map generation

The platform accepts standard OCT image sequences acquired in current clinical practice as input [26]. Following intravascular

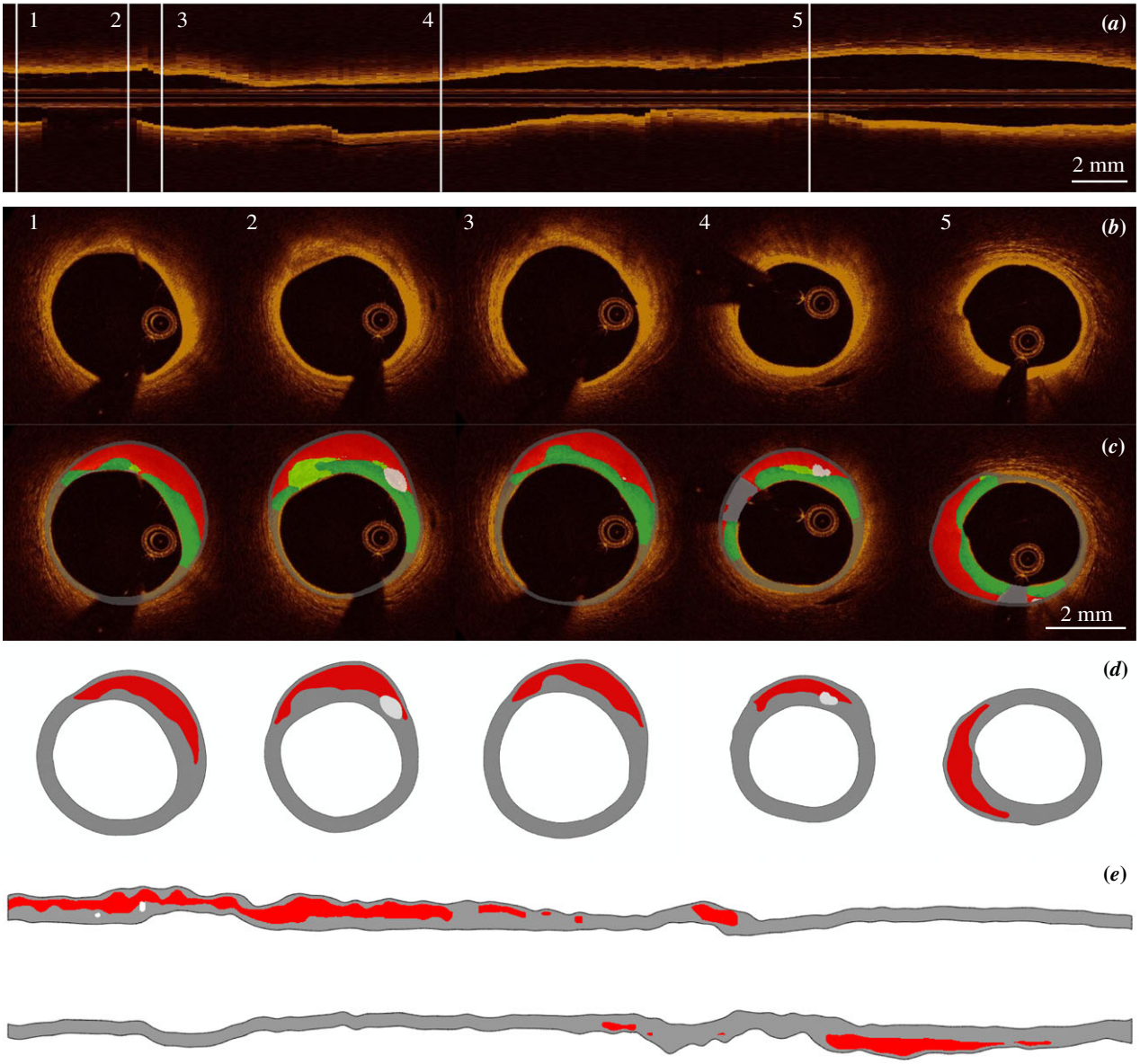

Figure 2. The outputs for geometrical model generation. (*a*,*b*) Longitudinal and cross-sectional OCT data are first acquired. (*c*) Image pixels are then automatically classified into healthy tissue (grey), lipid (red), calcium (white), fibrous tissue (dark green) and mixed tissue (light green) to produce segmented label maps of the lesion. (*d*,*e*) Label maps are semi-automatically transformed into a high-fidelity patient-specific 3D model with healthy tissue, lipid and calcium components.

image acquisition, the vessel wall is delineated using a previously reported automated methodology [27]. In brief, the utility fits a continuous 3D anisotropic elastic mesh to visible segments of the inner (lumen) and outer (external elastic lamina, representing the transition between media and adventitia) vessel borders, identified through automated image processing of the image sequence. A map of the pathological intimal and medial layers of the vessel wall is correspondingly obtained from the border information. The pathological regions are then provided to a convolutional neural network architecture detailed by Athanasiou *et al*. [28]. This network classifies each pixel in the lesion region of interest as belonging to one of five classes: calcium, lipid, fibrous tissue, mixed tissue or shadow (figure 2). Finally, the label map is post-processed to improve continuity and amenability to geometry construction. Specifically, spatial consistency is enhanced through 3D mode filtering using a $5 \times 5 \times 3$ voxel kernel. Subsequently, non-calcified plaque components smaller than 0.15 mm^2 in plane are replaced by the most common neighbouring tissue type. The calcium component is not subject to the size filtration process as the majority of identified calcium in such lesions is small in size [29]. To avoid the rare non-physiological scenario of lumen-facing lipid in the tissue map, such cases are automatically detected and a cap is added with a thickness of 200 µm (the mean fibrous cap thickness commonly measured *in vivo* [30]). All operations are performed in Matlab (MathWorks, Natick, MA, USA).

2.1.2. Geometry creation

Once the label maps are obtained, the spatial distribution of tissue is transformed into continuous 3D geometries. In this study, the fibrous and mixed tissue types are treated as healthy artery tissue to simplify 3D model construction, rendering a lesion that includes calcified and lipidic tissue components. The calcium components in the segmentation map are then dilated by 1 pixel to facilitate smooth intersection with lipid components in the 3D volume creation phase. The degree of dilation is minimal and is not expected to meaningfully affect the reconstructed geometries. After pre-processing, smoothed isolines surrounding isolated components of lipid and calcium are extracted. The inner and outer vessel wall borders are extracted in the same fashion. Spatial coordinates of these isolines are then used to generate stacks of 2D surfaces of each plaque component using Gmsh [31]. Within this process, a minimal

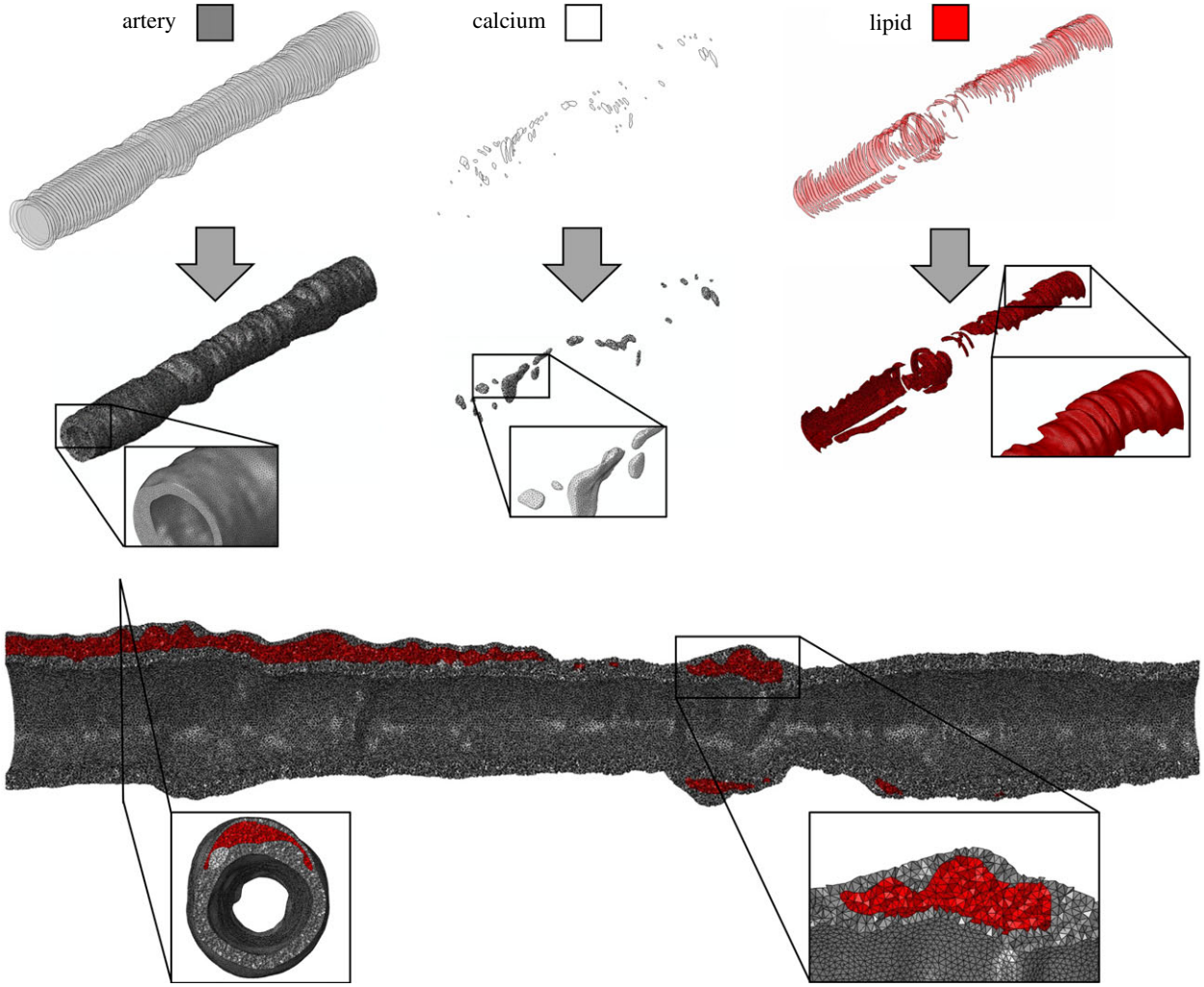

Figure 3. Overview of the 3D model generation process. Starting from a set of 2D surfaces (top), each material component is manually constructed as an independent 3D volume. A series of Boolean operations are conducted between all tissue components to ensure cohering boundaries and to avoid duplicate surfaces. The geometric model is then meshed to produce a global coarse model of the patient-specific lesion (bottom). Following global simulation, submodels are subsequently constructed from segments of the same geometric model and used as the basis for higher fidelity structural simulations.

Table 1. Hyperelastic material properties for the lipid and arterial tissue components.

material	C_{10} (kPa)	C_{01} (kPa)	C_{20} (kPa)	C_{11} (kPa)	C_{30} (kPa)	D
artery	127.9	0	0	0	0	0.096
lipid	1.6	0	9.3	0	11	0

intima–media thickness of 0.5 mm is enforced, compensating for instances where non-pathological tissue is rendered to be excessively thin by the border detection methodology.

The 2D contours for the lipid, calcium, lumen and healthy artery are then imported into SpaceClaim (ANSYS, Canonsburg, PA, USA) and employed to produce 3D volumetric plaque components through 3D surface interpolation methods. The curvature of the vessel is not taken into account for simplification purposes. A series of Boolean operations are then applied to the volumetric components, removing overlapping volumes and ensuring continuity between components within the vessel wall. The ultimate product is a continuous and smooth 3D model of the vessel encompassing the heterogeneous distribution of lipid and calcium within the diseased vessel wall (figure 3).

2.1.3. Material models

While the FE model generated here is amenable to any material model assignment, for demonstration and evaluation purposes, relatively simple isotropic constitutive mechanical models are used. Specifically, the material model for healthy tissue is designated to be hyperelastic and neo-Hookean, with a third-order polynomial strain energy function used for the lipid:

$$\psi = C_{10}(I_1 - 3) + C_{01}(I_2 - 3) + C_{20}(I_1 - 3)^2 + C_{11}(I_1 - 3)(I_2 - 3) + C_{30}(I_1 - 3)^3 + \frac{1}{D}(J - 1)^2, \tag{2.1}$$

where C_{ij} and D denote the material constants for distortional and compressional response and I_1, I_2 and J represent the first, second and third invariants of the right Cauchy–Green deformation tensor, respectively. The model parameters (table 1) are adopted from published literature within which *ex vivo* mechanical testing has quantified tissue material properties [32,33]. Calcium is assigned to be a linear elastic material:

$$\sigma = E \cdot \epsilon, \tag{2.2}$$

with a Young's modulus E of 184 MPa [34] and an assumed Poisson's ratio ν of 0.495.

2.1.4. Meshing and modelling

The artery geometry is meshed with second-order hybrid tetrahedral elements, where nodes at the interface boundaries between different materials are shared between components such that no contact algorithm is employed. Hybrid elements were chosen to allow incompressible material formulations, and second-order elements were chosen to improve accuracy. The resulting mesh is then used as the basis for a structural model that consists of a patient-specific multi-material coronary artery pressurized to physiological conditions. Boundary conditions are applied such that artery caps are fixed in all directions and the inner (i.e. luminal) surface is assigned an outwards pressure of 110 mmHg (15 kPa). The structural simulation is solved with ABAQUS/Implicit 6.13 (Dassault Systemes, Providence, RI, USA).

To ensure proper resolution of the stress distribution for the intricate lesion, a node-based submodelling technique is employed which applies a displacement boundary condition to a smaller and more finely meshed submodel of the lesion according to a simulated coarse mesh global model. Submodelling has proven to be a robust and reliable technique to minimize the computational costs while accurately resolving stresses and strains at specific regions of interest in large and complex atherosclerotic lesions [29,35]. The stress results from the global model inform the choice of submodel location, with areas of high stress denoting regions of interest to be selected for adaptive submodelling.

To determine sufficient mesh density for the submodel, the healthy artery default mesh size is set to a value of 0.1 mm and the surface of the plaque components is ascribed a smaller mesh edge length (0.05 mm) to fully resolve the complex lesion morphology. The edge length in the vicinity of the plaque surfaces is controlled by a distance function to ensure a gradual transition in mesh size. The submodel caps are given displacement boundary conditions according to the global model and similarly pressurized to 110 mmHg. Once a submodel is selected and simulated, the stress maps are used to adaptively remesh high-stress regions with an even finer mesh. Multiple tiers of stress-based meshing are used in which the level of refinement varied with the magnitude of the stress. The adaptive, stress-based remeshing process is repeated multiple times to ensure that there are no unresolved stress concentrations. Such comprehensive meshing techniques ensure a properly resolved stress field while also constraining the total mesh size of the submodel to manageable levels.

2.2. Computational case study

To demonstrate the viability of the developed platform, OCT data from a human coronary lesion were reconstructed with acquisition details described in our previous work [27]. The reconstructed vessel in question consists of the left anterior descending artery of a non-diabetic 65-year-old patient presenting with stable angina pectoris. The scan diameter, inter-frame resolution and axial resolutions were 10 mm, 200 µm and 15 µm, respectively. From the pullback dataset, a 40 mm section (200 frame series) was selected from a full pullback of 53.8 mm (269 frames); vessel borders were detected for the full segment, and every alternate frame (100 frames) was characterized by the described image-processing module. The model consisted of a patient-specific lesion with 12 lipid components, 23 calcium components and a continuous healthy artery component. The lesion consisted of approximately 38% healthy artery, 34% fibrous tissue, 3% mixed tissue, 24% lipidic tissue and 1% calcium tissue. In this specific model, the majority of the calcific components were localized away from the lumen within the intimal layer. For the coarse artery model, a general element edge length of 0.1 mm was found to sufficiently resolve the complex lesion morphology and produce sufficiently converged displacement results (preliminary analysis indicated less than a 5% change in displacement when mesh size is halved). The resulting mesh size was generated with approximately 1.7×10^6 second-order hybrid tetrahedral elements. After the coarse model was simulated, three submodels of 8 mm length each were selected for further investigation, with lengths chosen to mitigate boundary condition effects in regions of interest. The final mesh for both submodels consisted of approximately 0.6×10^6 elements.

2.2.1. Computational model variation

Conventionally, *in vivo* patient-specific 3D mechanical models of coronary atherosclerotic lesions focus primarily on the role of lipid tissue [23,24], as it is considered the most prevalent and spatially extended component associated with plaque structural stability. Accordingly, including calcium in tandem with lipid enables the detailed investigation of how calcium and lipid constituents interact in a synergistic or antagonistic fashion to affect the mechanical response of coronary lesions. To highlight the importance of considering multi-material models in a 3D FE simulation, a material inclusion variation analysis was implemented. Specifically, four model variants were created: a full multi-material model, in which both lipid and calcium material properties were assigned; and three hypothetical alternatives wherein diseased tissue types were reassigned to healthy tissue, yielding a model that is non-pathological as well as a calcium-only and a lipid-only model. The global model mesh for all four scenarios was identical, differing only in element material assignment to facilitate direct comparisons.

2.2.2. Quantitative stress analysis

Three illustrative transverse cross-sections were also selected to display scenarios in which calcium–lipid interactions were visually evident, or where TCFA-like morphologies could be identified. To conduct a quantitative comparison between the four computational model variations for each cross-section, a set of 180 equally spaced radial projections from the luminal centroid were defined for each analysed frame. The von Mises stress distribution along each projection was extracted. These data were used to assess the polar distribution of the luminal stress (defined as stress induced on the inner vessel border) and the maximum mural stresses (defined as the maximum stress along the projection within the healthy artery tissue component) for each specified frame. The same methodology was applied to analyse the variation in maximal mural arterial stress along the longitudinal direction. For each geometric submodel, 40 radial paths were defined along the longitudinal direction of the artery and were used to extract the von Mises stress distribution across the vessel wall. The process was repeated for each computational model material variation to compare the effect of different material inclusions on the variation of stress along the artery.

Furthermore, a larger statistical analysis was carried out over an extended number of submodel frames, in which the effects of including lipidic and calcific tissue in isolation were quantified. For the analysis of lipid, 30 frames for each submodel were chosen for quantification. In total, 90 cross-sections of the non-pathological model and lipid-only model were each analysed using the radial projection method with 3° separating the individual projections from one another. In each frame, the minimum cap thickness (defined as the minimum distance between the lipid and lumen) was selected and the maximum von Mises tissue stress along the equivalent radial projection was extracted. The relationship between the maximum tissue stress at the site of minimum cap thickness and the magnitude of minimum cap thickness was then

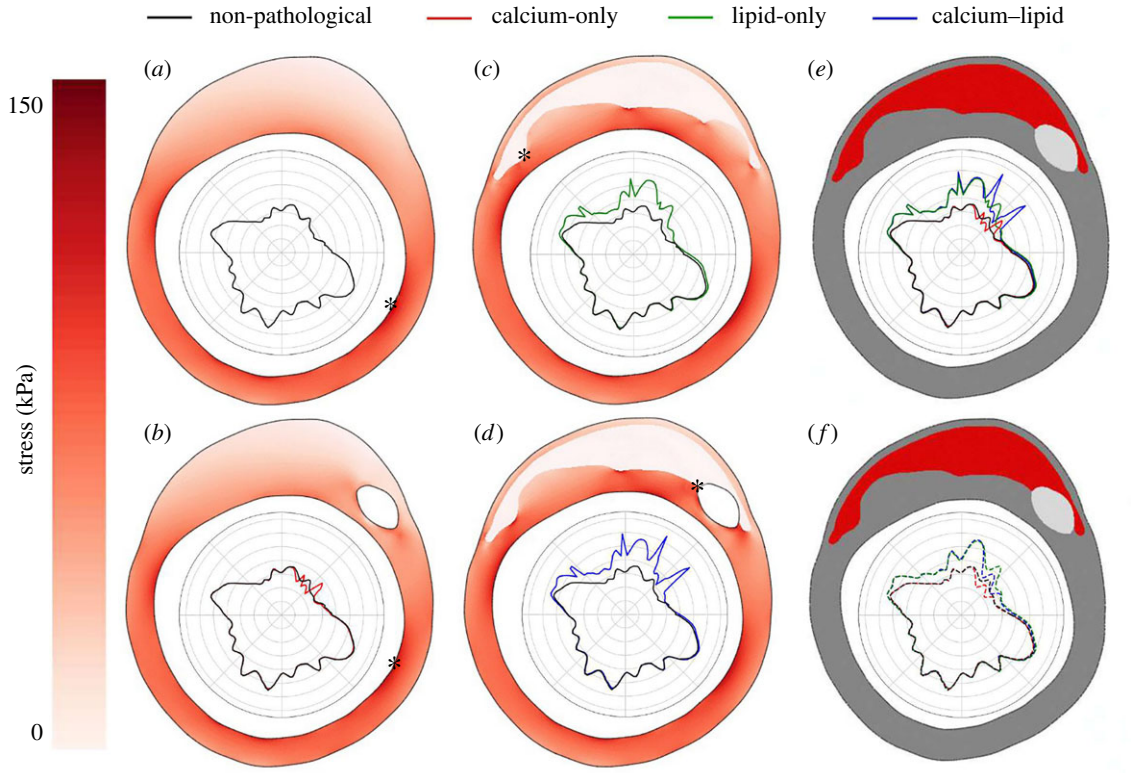

Figure 4. Representative cross-section detailing the von Mises stress distribution, together with maximum mural stress as a function of circumferential position as shown in the polar plots. Calcium and lipid can exhibit opposing effects on plaque stability in isolation and synergistic effects in tandem. Data shown for model variations containing (*a*) only arterial tissue, (*b*) arterial tissue and calcium, (*c*) arterial tissue and lipid, and (*d*) arterial tissue, calcium and lipid. (*e*) Maximum tissue stress (solid lines) and (*f*) luminal stress (dashed lines) highlight differences in results yielded by the four variations. The locations of maximum stress are indicated by the (*) marker. The polar plot axis range is equivalent to that of the colourbar. Calcium was excluded from the visualization to increase clarity of arterial stress distribution.

displayed in a scatterplot for both models. For the calcium, 34 cross-sections (chosen manually because of limited availability of calcium) of the non-pathological model and the calcium-only model were analysed using a set of radial projections with 0.5° of angular separation. The relationship between maximum tissue stress along each radial projection and the corresponding arc angle (defined as the angular distance from the centre of the calcium component within the cross-section) was then displayed in a scatterplot.

3. Results

In total, four global model simulations were conducted to compare the effect of various lesion components. Each global model was used to create three submodels. Each submodel was then simulated and adaptively remeshed three times recursively, such that a total of 36 simulations were performed. Each global model simulation took 6 h of simulation time and the maximum time that a submodel simulation required was 18 h.

3.1. Effect of lipid on stress distribution

The effect of including lipid on the stress distribution is shown in figures 4–8. In the non-pathological model (figure 4*a*), the stress concentrates at a location of minimal wall thickness. However, once lipid is included (figure 4*c*), high stresses instead concentrate at the adluminal lipid–tissue interface. The inclusion of lipid tissue also shifts the location of the maximum arterial tissue stress to the thin cap structure, increasing the maximum within-frame arterial tissue stress from 118 to 125 kPa (figure 4*a*,*c*). As apparent in the polar plots of the maximum and inner surface stresses, the addition of the lipid increases the maximum arterial tissue stress and amplifies the inner border stress distribution in regions which contain lipid (up to 80% for maximum stress and 60% for surface stress), though the inclusion of lipid does not affect stress fields in lipid-free regions (figure 4*f*,*e*). This trend is also evident in the TCFA-like cross-section (figure 5*b*), where the addition of lipidic components not only increases the arterial tissue stress (up to 140% for maximum stress and 110% for surface stress) but also shifts the location of maximum within-frame stress to the thin cap structure (elevating stresses from 110 kPa in figure 5*a* to 196 kPa in figure 5*b*). In instances where the lipid is covered by a thick fibrous cap (as exemplified in figure 6*c*, with a minimum cap thickness of 160 µm), the inclusion of lipidic tissue does not shift the location of maximum within-frame stress. However, it does have an evident effect on intraplaque stress distributions, as shown in the corresponding polar plots. Specifically, maximum arterial tissue stress and inner border stress are both slightly amplified with the inclusion of lipid tissue (up to a 40% increase for maximum arterial stress and a 20% increase for surface stress, seen in figure 6*e*,*f*, respectively). Corroborating these trends, the 3D stress distributions highlight how both luminal (figure 7) and mural (figure 9*a*–*c*) stresses are elevated at the site of intraplaque lipid. Lastly, the quantitative analysis of including lipid (figure 8*b*) reveals that the addition of lipid tissue causes a significant increase in maximum arterial tissue stress at the point of minimum cap thickness within each frame. Furthermore, the increase in stress induced by adding lipid exhibits an exponential relationship with minimum cap thickness, as indicated by the logarithmic fit.

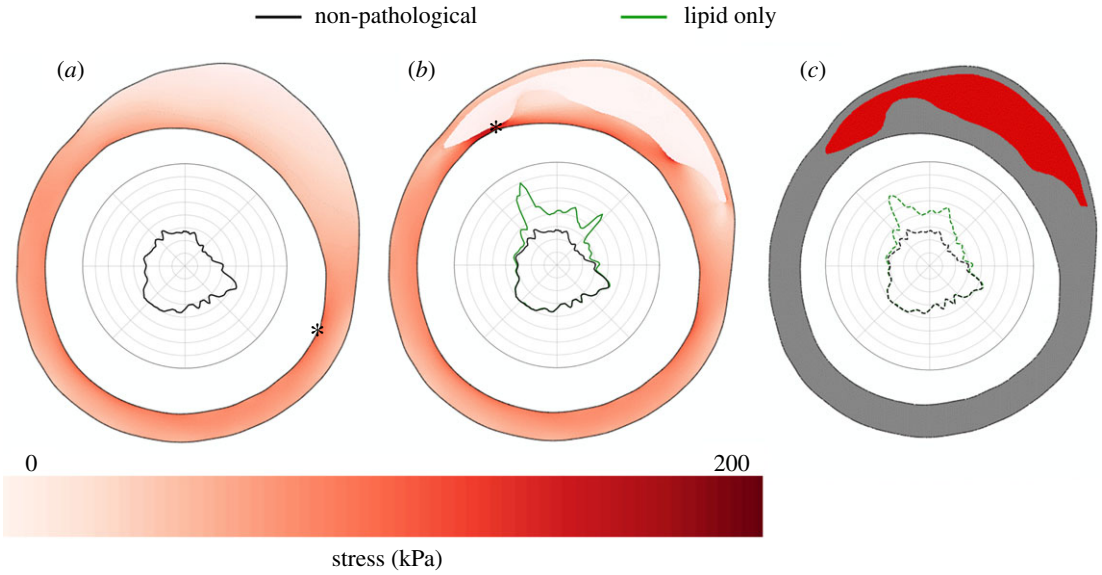

Figure 5. Representative cross-section detailing the distribution of von Mises stress, together with corresponding polar plots of maximum von Mises stress as a function of circumferential position. TCFA-like structures (minimum fibrous cap thickness equal to 75 µm) concentrate mechanical stress at the thin cap region. Output for model variation containing (*a*) only arterial tissue and (*b*) arterial tissue and lipid. The absence of calcium in proximity to this frame made other model variations redundant. (*c*) Luminal stress (dashed lines) highlights differences in the results of the two variations. The locations of maximum stress are indicated by the (*) marker. The polar plot axis range is equivalent to that of the colourbar.

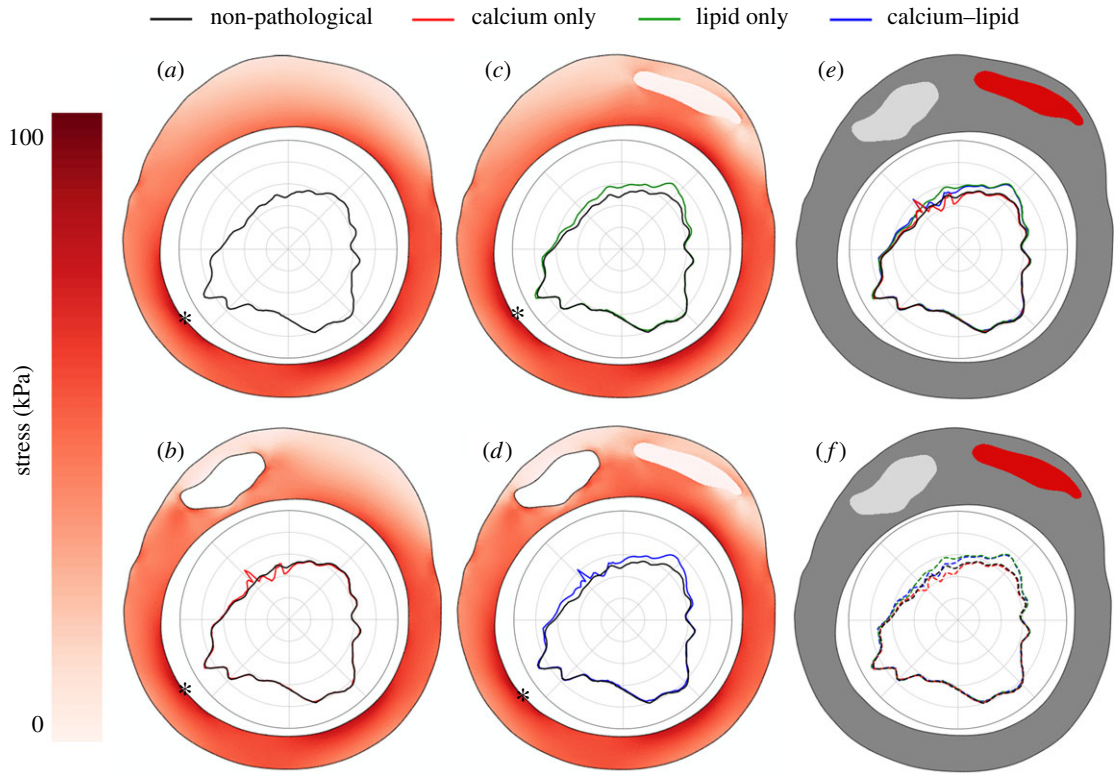

Figure 6. The von Mises stress, together with corresponding polar plots of maximum von Mises stress as a function of circumferential position, plotted for a representative cross-section. Stress distributions show that the lipid and calcium can have antagonistic interaction effects even if the components do not share an interface or point of contact. Cross-section shows an instance where lipid and calcium have seemingly interactive effects on the micro-mechanical environment. Data shown for model variations containing (*a*) only arterial tissue, (*b*) arterial tissue and calcium, (*c*) arterial tissue and lipid, and (*d*) arterial tissue, calcium and lipid. (*e*) Maximum tissue stress (solid lines) and (*f*) luminal stress (dashed lines) highlight differences in results for the four variations. The locations of maximum stress are indicated by the (*) marker. The polar plot axis range is equivalent to that of the colourbar. Calcium was excluded from the visualization to increase clarity of arterial stress distribution.

3.2. Effect of calcium on stress distribution

The inclusion of calcific components increases stresses at the major (circumferential) axis poles (up to 30%; figure 6*b*), while decreasing stresses at the minor (radial) axis poles (by as much as 30%; figure 4*b*). These stress concentrations are also apparent in the maximum arterial tissue stress polar plots, where elevated maxima in von Mises stress visually correspond to the position of the major axis poles (figure 4*b*). As illustrated in the surface stress polar plots of figures 4*f* and 6*f*,

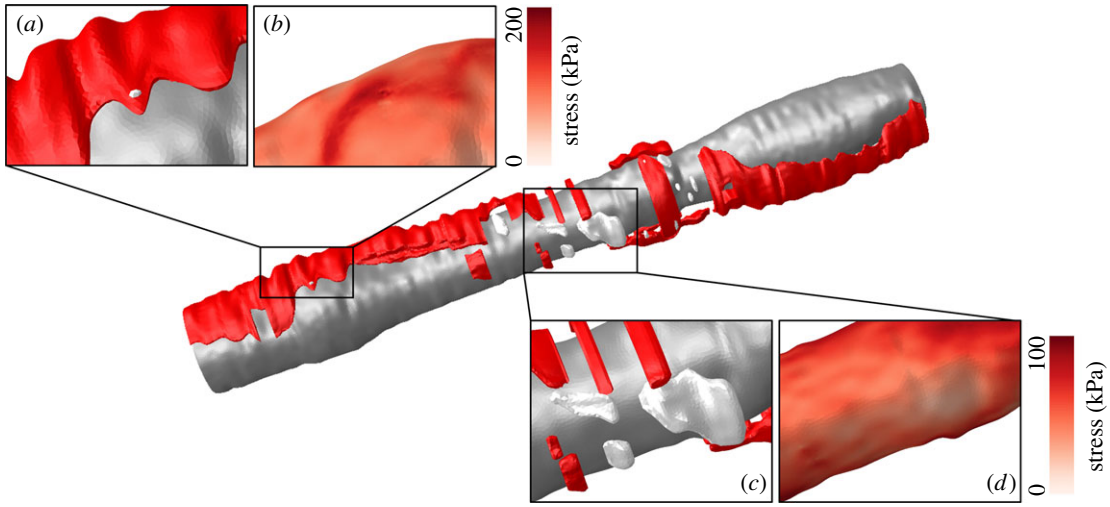

Figure 7. Three-dimensional representation of the calculated stress distribution provided by the computational model. As indicated qualitatively by the expanded inset sections, lipid entities (red) can be associated with increased surface stress near the shoulder region. On the contrary, calcium (white) seemingly decreases underlying surface stress. (*a*) and (*c*) show the model in greater detail; (*b*) and (*d*) show a rendering of the underlying surface stress, using different stress scales to highlight important features. For clarity, only the lipid, calcium and luminal surface are shown.

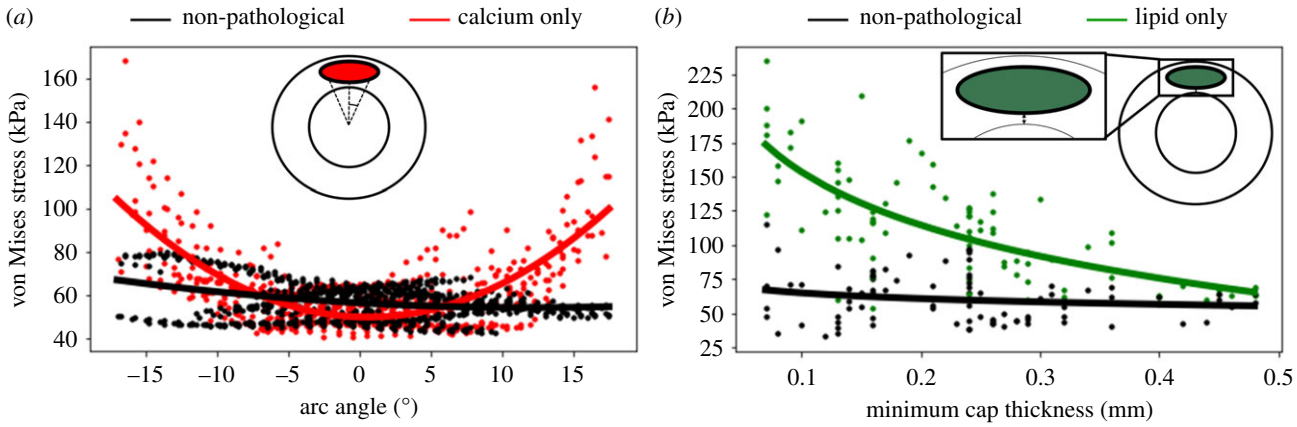

Figure 8. Quantitative analysis plots demonstrating the contribution of different intraplaque components on the resulting mechanical response. (*a*) Regional plaque structural stress levels are suppressed at the centre of the calcification arc but elevated at its edges, as indicated by the addition of calcific entities (red) to the simplified non-pathological model (black). (*b*) Stress levels are amplified at the underlying luminal surface, indicated by the addition of lipidic plaque entities (green) to the simplified non-pathological model (black).

including calcium also causes the luminal stress at the minor axis poles in the juxtaluminal region to decrease below that of the non-pathological model by 20% for both frames. Including calcium alone (i.e. in the absence of lipid) did not change the location or magnitude of the maximum within-frame arterial tissue stress in figure 4*a*,*b* (117 kPa) or figure 6*a*,*b* (90 kPa). The 3D stress distribution on the inner surface of the artery illustrates that including calcium components (figure 7*c*) induces a stress-diminishing effect on the underlying inner surface stress (figure 7*d*), which corresponds to the minor axis pole in a cross-sectional view. The longitudinal stress plots in figure 9*a*,*b* shows that the presence of both in-frame and out-of-frame calcium induces a minor stress-diminishing effect. Assessing derived stresses throughout the entire model, the relationship between maximum tissue stress along each radial projection was plotted against the corresponding projection arc angle (figure 8*a*). The scatterplot shows how the inclusion of calcium introduces a decrease in maximum tissue stress with low arc angles (corresponding to the centre of the calcium at the radial poles). The maximum stress then increases significantly at the calcium periphery (approaching the circumferential poles), where the stress seems to rise with arc angle as indicated by the parabolic curve fit.

3.3. Effect of lipid–calcium interaction on stress distribution

Including calcium and lipid imposes an interaction effect on the stress distribution (figure 4*d*) where the stress concentrations at the major axis poles of a calcium component are amplified in magnitude with the addition of an encompassing lipid core (up to a 120% increase for maximum arterial tissue stress and a 60% increase for surface stress). Furthermore, the maximum arterial tissue stress plot shows that, while the major axis poles of the embedded calcium are sites of stress concentration, the juxtaluminal region at the calcification minor axis pole bears a higher amount of stress than both the non-pathological model and the calcium-only model, as well as a lower amount of stress than the calcium-only model (figure 4*e*). Figure 6*d* shows another representative example where lipidic and calcific components are both present without being in physical contact. Here, the maximum

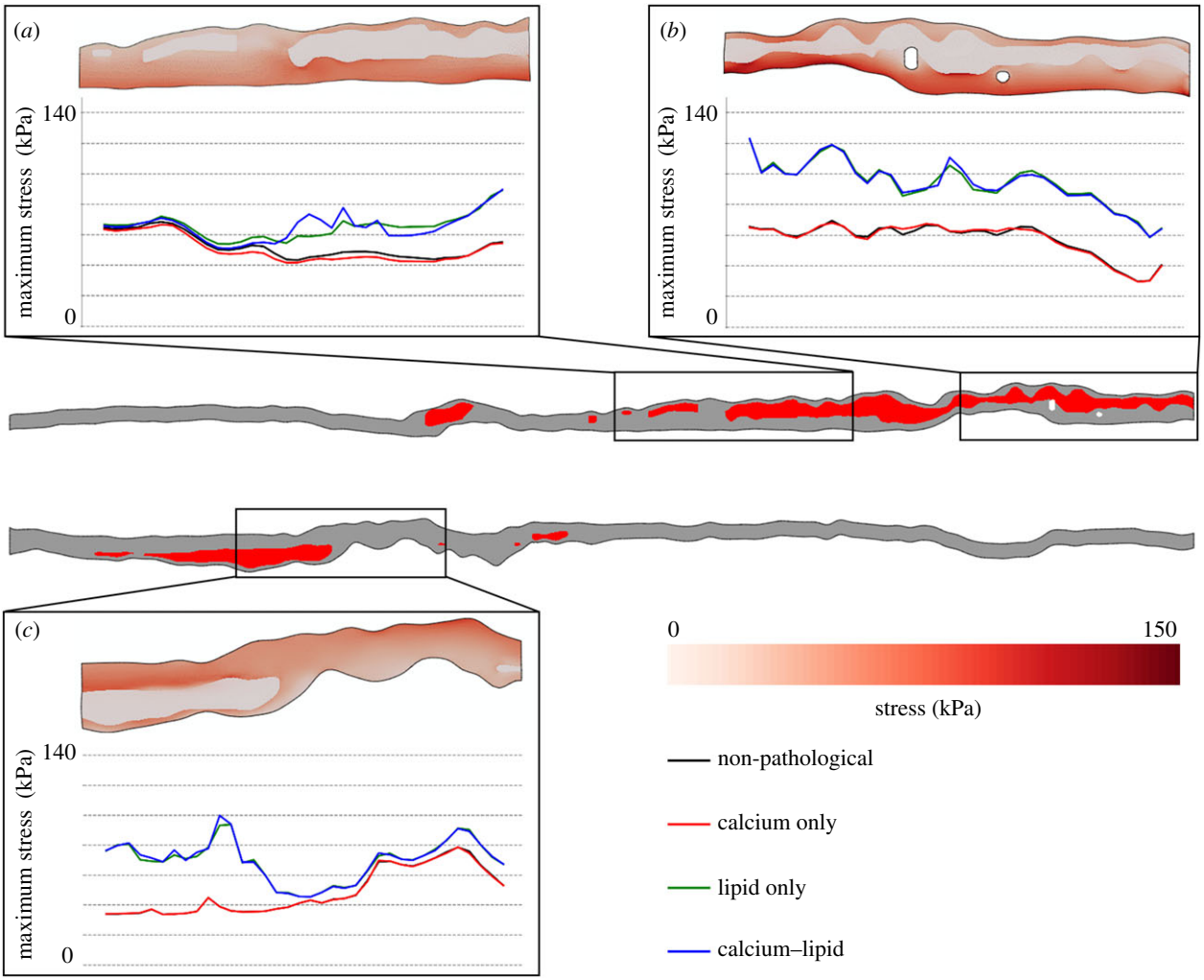

Figure 9. Two-dimensional representation of the calculated arterial von Mises stress distribution within longitudinal cut-planes. Expanded insets shows stress distribution throughout the calcium–lipid model's vessel wall for multiple submodels (*a–c*). Also shown for each submodel is the maximum arterial tissue stress as a function of longitudinal position for each model variation. Longitudinal stress plots show a strong relationship between the presence of lipid and increased stress along the longitudinal direction, while calcium is associated with decreased stress and displays interaction effects with lipid. In-frame calcium was excluded from the visualization to increase clarity of arterial stress distribution. Stress results 0.4 mm from the boundaries of each submodel were excluded to avoid boundary effects.

arterial tissue stress is seemingly elevated in the region between the tissue components (10% increase) compared with both the non-pathological and calcium-only (15% decrease) model, and slightly diminished compared with the lipid-only (20% increase) model. The longitudinal stress plot in figure 9*a* suggests an interaction effect between the out-of-frame calcium and within-frame lipid, as evidenced by the stress concentrations occurring near the centre of the plot.

Lastly, while all of the above sections have been focusing on the variation in maximal von Mises stress due to its potential clinical relevance, it must be noted that the analysis of mean stress and thus the transfer of mechanical load throughout the vessel wall exhibits more subtle variation. Nevertheless, a detailed assessment of how mean stress varies with the addition of various tissue inclusions will have to be conducted in future studies, partially because of the fact that a mean effective stress metric—being averaged in all spatial directions—cannot adequately describe the directional transfer of mechanical force.

4. Discussion

In this study, a platform for 3D structural plaque modelling has been presented in which clinical intravascular images are utilized to create patient-specific arterial geometries with multi-material recovery. These reconstructions are then used for structural simulations, resolving local mechanical response with high fidelity. These structural model representations can be leveraged for a variety of purposes, such as studying how the 3D morphology of different plaque components modulates structural stability, or how clinical interventions might alter the resulting mechanical response.

As previous OCT-based reconstructions of atherosclerotic arteries have primarily relied on the manual delineation of vessel borders and plaque components from acquired images [21,23], they require significant time investment from trained clinical staff and are subject to inter-reader variability. To mitigate such limitations, multi-modality approaches have been implemented wherein the outer border information is obtained from co-registered IVUS frames [22,24], necessitating multi-modality clinical data and image co-registration. Accordingly, a significant benefit and novelty of our platform lies in the use of automated image-processing utilities for vascular wall delineation and tissue classification, avoiding the need for manual segmentation and multi-modality imaging data.

Moreover, another advancement lies in the 3D nature of our proposed modelling platform. While coronary artery

rupture has been experimentally indicated to occur at approximately 300–500 kPa [36,37], 2D FE simulations tend to overestimate intraplaque stresses [14–16,38] with predictions of up to 1000 kPa reported in some previous 2D studies [22]. In contrast, our model predicts physiological levels of stress (200 kPa) that are below the reported threshold of 300–500 kPa, congruous with the few other 3D coronary models in the literature [23,24]. Furthermore, while a multitude of studies have examined the effects of plane strain assumptions for lipidic components [14,15], there have been no studies to our knowledge that examine how well this assumption holds with regards to calcium components, which can exhibit rapid morphological variation in the longitudinal vessel direction [39]. To study this effect, 3D modelling would thus be essential to reproduce accurate stress levels in the vicinity of calcific atherosclerotic components. It must also be noted that the homogeneous 3D artery model exhibits non-negligible variation in stress (figures 4*a*, 5*a* and 6*a*). While the source of this variation can be seen as the result of the vessel's in-plane geometric variation in vessel thickness, luminal diameter and curvature, it is also expected that the morphological variation along the longitudinal direction plays a definite role in the arterial mechanical response, which further emphasizes the importance of 3D modelling in modelling more realistic outcomes.

Lastly, this framework allows for the incorporation of multiple plaque components in the structural simulation, where the interplay between different tissues and their unique impact on structural responses can be modelled. With different intraplaque components showing vastly different innate constitutive behaviour [33], the implementation of a multi-material model is therefore of particular importance for studying local stress patterns in patient-specific lesions. For example, such a complex model allows us to explore how lipid and calcium—being, respectively, softer and stiffer than surrounding vascular tissue—have opposing roles in defining the local mechanical response. These trends are demonstrated in the produced results, where the softer lipid components concentrate stresses in the juxtaluminal fibrous cap (figures 4*c*, 5*b*, 6*c*, 7*b* and 9*a–c*), with values elevated compared with the homogeneous equivalent. Contrarily, the stiffer calcium tends to dissipate stresses in the radially positioned juxtaluminal tissue, while amplifying stress in the vicinity of the major axis poles of the calcification (figures 4*b*, 6*b*, 8*a* and 9*b*). As such, considering the investigated tissue classes in isolation, lipid and calcium seem to redistribute intraplaque stresses in opposing manners (figures 4 and 6) and play different but important roles in modulating plaque structural stability.

However, the most complex interactions produced by this platform are observed when calcium and lipid are considered together, where synergistic or antagonistic interactions are induced depending on the geometric configuration of both components. The inclusion of an embedded calcium into a lipid component creates a 3D zone of concentrated stress around the region where healthy artery, lipid and calcium intersect (figure 4). Such stress concentrations may be clinically relevant when considering the probability of plaque rupture or progression. By contrast, when a calcium component is included some distance away from the lipid component, the region of artery in between both components experiences both an increase in stress due to the lipid component as well as a decrease in stress due to the calcium component (figure 6), possibly stabilizing a lesion that would rupture otherwise. It is likely that such multi-material interaction effects are a complex result of both component positioning and morphology, where the quantitative investigation of such phenomena and their clinical relevance requires further attention.

Despite being a promising engineering tool capable of exploring the structural response of atherosclerotic lesions, this platform bears a number of limitations. First, the presented platform lacks access to patient-specific material properties. For the inclusion of such, image-based inverse modelling could be utilized to obtain patient-specific material properties [33]. Alternatively, complementary image data could be included in the platform. For example, recent advances in polarization-sensitive OCT have been shown to provide information on the fibrous composition of an assessed lesion plaque [40]. However, even though absolute stress magnitudes may vary as a function of defined constitutive parameters, the relative stress distribution and innate effects of lipid and calcium are expected to be similar to what was observed in our study.

Second, the lesion modelled in our study was of a predominantly lipidic nature, with only minor calcific entities dispersed along the 3D model. As coronary calcium exhibits a wide array of morphological phenotypes [39], inferring the comprehensive clinical influence of calcium will require further modelling. However, the presented platform offers unique abilities for such systematic model analysis, where models with varying degrees of calcium could be generated to observe potential mechanical trends and interaction effects with concomitant lipid pools. Furthermore, although we believe the derived mechanical patterns in our model to be indicative of general intraplaque stress distribution in the presence of calcium and lipid deposits, specific behaviour relating to luminal-facing or more deep deposits would have to be assessed in separate future studies.

Third, as the reconstruction is based on OCT images alone, the patient-specific artery is currently modelled as a straight entity with no information on vessel curvature included in the geometry construction. Curvature and bending effects have been shown to be important in obtaining accurate stress predictions in coronary plaques. Specifically, the direction and degree of bending can cause FE predictions using straight model formulations to overestimate or underestimate the stress [41]. While this effect is not expected to be critical for vessels that are relatively straight, tortuous coronary vessels may require curvature to be included for more accurate stress estimation. Accordingly, vessel curvature can be integrated into the computational platform detailed above with the availability of 3D coronary angiography centreline data.

Finally, the structural modelling strategy detailed in this study pressurizes the *in vivo* geometry acquired from the OCT data to 110 mmHg and thus does not include residual and initial stresses. While such assumptions have been shown to be influential on the resulting arterial stress distributions [42], implementing residual and initial stresses is restricted for clinical models based on the inherent limitations of *in vivo* data. Typically, arterial residual stresses are modelled in pathological studies by making a longitudinal incision along the artery and noting the opening angle [43]. However, this method is not available for *in vivo* studies,

and obtaining the residual stress through computational optimization methods is still an active area of research [44].

5. Conclusion

This study details the use of a computational platform generating high-fidelity multi-material patient-specific models of atherosclerotic lesions using *in vivo* OCT images as sole input. These semi-automatically produced models are then used as the basis for structural simulations to recapitulate the complex mechanical response of the lesion and investigate how the heterogeneity of the lesion modulates plaque structural stability. This study further demonstrates the importance of including both calcium and lipid in the coronary artery model formulation through the conduction of a computational case study. The simulated results suggest that, when considered in isolation, the lipid and calcium components exhibit important and opposing effects on the stress field. Furthermore, when considered in tandem, they exhibit complex synergistic or antagonistic interaction effects on the stress field, depending on their relative positioning and morphology. These findings illustrate the importance of high-fidelity and patient-specific lesion reconstruction in assessing lesion micro-mechanics, and the potential for more comprehensive and accurate assessment of stress distributions in advancing the utility of such computational models.

Data accessibility. Owing to IRB limitations, the intravascular images that are used as input data for this study cannot be made publically available. The code used in this study is available at: https://doi.org/10.5281/zenodo.5151216.

Authors' contributions. M.L.O., D.M., E.R.E. and F.R.N. designed the study; K.K. conducted the experiments; K.K., M.L.O., D.M. and F.R.N. analysed the results. All authors reviewed the manuscript.

Competing interests. We declare we have no competing interests.

Funding. Funding for this study has been received from the National Institutes of Health (grant no. GM 49039), the Mathworks Fellowship and the Alice and Knut Wallenberg Foundation.

References

1. Stone GW *et al.* 2011 A prospective natural-history study of coronary atherosclerosis. *N. Engl. J. Med.* **364**, 226–235. (doi:10.1056/NEJMoa1002358)
2. Naghavi M *et al.* 2003 From vulnerable plaque to vulnerable patient: a call for new definitions and risk assessment strategies: part I. *Circulation* **108**, 1664–1672. (doi:10.1161/01.CIR.0000087480.94275.97)
3. Burke AP, Kolodgie FD, Farb A, Weber D, Virmani R. 2002 Morphological predictors of arterial remodeling in coronary atherosclerosis. *Circulation* **105**, 297–303. (doi:10.1161/hc0302.102610)
4. Calvert PA *et al.* 2011 Association between IVUS findings and adverse outcomes in patients with coronary artery disease: the VIVA (VH-IVUS in Vulnerable Atherosclerosis) Study. *JACC: Cardiovasc. Imaging* **4**, 894–901. (doi:10.1016/j.jcmg.2011.05.005)
5. Cheng GC, Loree HM, Kamm RD, Fishbein MC, Lee RT. 1993 Distribution of circumferential stress in ruptured and stable atherosclerotic lesions. A structural analysis with histopathological correlation. *Circulation* **87**, 1179–1187. (doi:10.1161/01.CIR.87.4.1179)
6. Lee RT, Schoen FJ, Loree HM, Lark MW, Libby P. 1996 Circumferential stress and matrix metalloproteinase 1 in human coronary atherosclerosis: implications for plaque rupture. *Arterioscler. Thromb. Vasc. Biol.* **16**, 1070–1073. (doi:10.1161/01.ATV.16.8.1070)
7. Hallow KM, Taylor WR, Rachev A, Vito RP. 2009 Markers of inflammation collocate with increased wall stress in human coronary arterial plaque. *Biomech. Model. Mechanobiol.* **8**, 473–486. (doi:10.1007/s10237-009-0151-8)
8. Athanasiou L, Nezami FR, Edelman ER. 2018 Position paper computational cardiology. *IEEE J. Biomed. Health Inform.* **23**, 4–11. (doi:10.1109/JBHI.2018.2877044)
9. Corral-Acero J *et al.* 2020 The 'digital twin' to enable the vision of precision cardiology. *Eur. Heart J.* **41**, 4556–4564. (doi:10.1093/eurheartj/ehaa159)
10. Tang D *et al.* 2014 Image-based modeling for better understanding and assessment of atherosclerotic plaque progression and vulnerability: data, modeling, validation, uncertainty and predictions. *J. Biomech.* **47**, 834–846. (doi:10.1016/j.jbiomech.2014.01.012)
11. Teng Z *et al.* 2014 Coronary plaque structural stress is associated with plaque composition and subtype and higher in acute coronary syndrome: the BEACON I (Biomechanical Evaluation of Atheromatous Coronary Arteries) Study. *Circulation: Cardiovasc. Imaging* **7**, 461–470. (doi:10.1161/CIRCIMAGING.113.001526)
12. Costopoulos C, Huang Y, Brown AJ, Calvert PA, Hoole SP, West NE, Gillard JH, Teng Z, Bennett MR. 2017 Plaque rupture in coronary atherosclerosis is associated with increased plaque structural stress. *JACC: Cardiovasc. Imaging* **10**, 1472–1483. (doi:10.1016/j.jcmg.2017.04.017)
13. Ohayon J, Teppaz P, Finet G, Rioufol G. 2001 *In-vivo* prediction of human coronary plaque rupture location using intravascular ultrasound and the finite element method. *Coron. Artery Dis.* **12**, 655–663. (doi:10.1097/00019501-200112000-00009)
14. Ohayon J, Finet G, Treyve F, Rioufol G, Dubreuil O. 2005 A three-dimensional finite element analysis of stress distribution in a coronary atherosclerotic plaque: in-vivo prediction of plaque rupture location. *Biomech. Appl. Comput. Assist. Surg.* **37**, 225–241. (doi:10.1097/00019501-200112000-00009)
15. Tang D, Yang C, Zheng J, Woodard PK, Sicard GA, Saffitz JE, Yuan C. 2004 3D MRI-based multicomponent FSI models for atherosclerotic plaques. *Ann. Biomed. Eng.* **32**, 947–960. (doi:10.1023/B:ABME.0000032457.10191.e0)
16. Nieuwstadt HA, Akyildiz AC, Speelman L, Virmani R, van der Lugt A, van der Steen AF, Wentzel JJ, Gijsen FJ. 2013 The influence of axial image resolution on atherosclerotic plaque stress computations. *J. Biomech.* **46**, 689–695. (doi:10.1016/j.jbiomech.2012.11.042)
17. Costopoulos C, Maehara A, Huang Y, Brown AJ, Gillard JH, Teng Z, Stone GW, Bennett MR. 2020 Heterogeneity of plaque structural stress is increased in plaques leading to MACE: insights from the PROSPECT Study. *JACC: Cardiovasc. Imaging* **13**, 1206–1218. (doi:10.1016/j.jcmg.2019.05.024)
18. Loree HM, Kamm R, Stringfellow R, Lee RT. 1992 Effects of fibrous cap thickness on peak circumferential stress in model atherosclerotic vessels. *Circ. Res.* **71**, 850–858. (doi:10.1161/01.RES.71.4.850)
19. Ohayon J *et al.* 2008 Necrotic core thickness and positive arterial remodeling index: emergent biomechanical factors for evaluating the risk of plaque rupture. *Am. J. Physiol.-Heart Circ. Physiol.* **295**, H717–H727. (doi:10.1152/ajpheart.00005.2008)
20. Moreno PR. 2009 The high-risk thin-cap fibroatheroma: a new kid on the block. *Circulation: Cardiovasc. Interv.* **2**, 500–502. (doi:10.1161/CIRCINTERVENTIONS.109.922146)
21. Chau AH *et al.* 2004 Mechanical analysis of atherosclerotic plaques based on optical coherence tomography. *Ann. Biomed. Eng.* **32**, 1494–1503. (doi:10.1114/B:ABME.0000049034.75368.4a)
22. Doradla P *et al.* 2020 Biomechanical stress profiling of coronary atherosclerosis: identifying a multifactorial metric to evaluate plaque rupture risk. *JACC: Cardiovasc. Imaging* **13**, 804–816. (doi:10.1016/j.jcmg.2019.01.033)

23. Wang J, Paritala PK, Mendieta JB, Komori Y, Raffel OC, Gu Y, Li Z. 2020 Optical coherence tomography-based patient-specific coronary artery reconstruction and fluid–structure interaction simulation. *Biomech. Model. Mechanobiol.* **19**, 7–20. (doi:10.1007/s10237-019-01191-9)
24. Guo X *et al.* 2018 Combining IVUS and optical coherence tomography for more accurate coronary cap thickness quantification and stress/strain calculations: a patient-specific three-dimensional fluid-structure interaction modeling approach. *J. Biomech. Eng.* **140**, 0410051–04100512. (doi:10.1115/1.4038263)
25. Guo X *et al.* 2019 A multimodality image-based fluid–structure interaction modeling approach for prediction of coronary plaque progression using IVUS and optical coherence tomography data with follow-up. *J. Biomech. Eng.* **141**, 0910031–0910039. (doi:10.1115/1.4043866)
26. Tearney GJ *et al.* 2012 Consensus standards for acquisition, measurement, and reporting of intravascular optical coherence tomography studies: a report from the International Working Group for Intravascular Optical Coherence Tomography Standardization and Validation. *J. Am. Coll. Cardiol.* **59**, 1058–1072. (doi:10.1016/j.jacc.2011.09.079)
27. Olender ML, Athanasiou LS, José M, Ben-Assa E, Nezami FR, Edelman ER. 2018 A mechanical approach for smooth surface fitting to delineate vessel walls in optical coherence tomography images. *IEEE Trans. Med. Imaging* **38**, 1384–1397. (doi:10.1109/TMI.2018.2884142)
28. Athanasiou LS, Olender ML, José M, Ben-Assa E, Edelman ER. 2019 A deep learning approach to classify atherosclerosis using intracoronary optical coherence tomography. In *Medical Imaging 2019: Computer-Aided Diagnosis*, vol. 10950, p. 109500N, Bellingham, WA: International Society for Optics and Photonics.
29. Maldonado N, Kelly-Arnold A, Vengrenyuk Y, Laudier D, Fallon JT, Virmani R, Cardoso L, Weinbaum S. 2012 A mechanistic analysis of the role of microcalcifications in atherosclerotic plaque stability: potential implications for plaque rupture. *Am. J. Physiol.-Heart Circ. Physiol.* **303**, H619–H628. (doi:10.1152/ajpheart.00036.2012)
30. Lv R *et al.* 2020 Using optical coherence tomography and intravascular ultrasound imaging to quantify coronary plaque cap thickness and vulnerability: a pilot study. *Biomed. Eng. Online* **19**, 1–18. (doi:10.1186/s12938-019-0745-z)
31. Geuzaine C, Remacle J-F. 2009 Gmsh: a 3-D finite element mesh generator with built-in pre- and post-processing facilities. *Int. J. Numer. Methods Eng.* **79**, 1309–1331. (doi:10.1002/nme.2579)
32. Karimi A, Navidbakhsh M, Faghihi S, Shojaei A, Hassani K. 2013 A finite element investigation on plaque vulnerability in realistic healthy and atherosclerotic human coronary arteries. *Proc. Inst. Mech. Eng. Part H: J. Eng. Med.* **227**, 148–161. (doi:10.1177/0954411912461239)
33. Noble C *et al.* 2020 Patient specific characterization of artery and plaque material properties in peripheral artery disease. *J. Mech. Behav. Biomed. Mater.* **101**, 103453. (doi:10.1016/j.jmbbm.2019.103453)
34. Ebenstein DM, Coughlin D, Chapman J, Li C, Pruitt LA. 2009 Nanomechanical properties of calcification, fibrous tissue, and hematoma from atherosclerotic plaques. *J. Biomed. Mater. Res. Part A* **91**, 1028–1037. (doi:10.1002/jbm.a.32321)
35. Leach JR, Rayz VL, Mofrad MR, Saloner D. 2010 An efficient two-stage approach for image-based FSI analysis of atherosclerotic arteries. *Biomech. Model. Mechanobiol.* **9**, 213–223. (doi:10.1007/s10237-009-0172-3)
36. Holzapfel GA, Sommer G, Gasser CT, Regitnig P. 2005 Determination of layer-specific mechanical properties of human coronary arteries with nonatherosclerotic intimal thickening and related constitutive modeling. *Am. J. Physiol.-Heart Circ. Physiol.* **289**, H2048–H2058. (doi:10.1152/ajpheart.00934.2004)
37. Claes E, Atienza JM, Guinea GV, Rojo FJ, Bernal JM, Revuelta JM, Elices M. 2010 Mechanical properties of human coronary arteries. In *2010 Annu. Int. Conf. of the IEEE Engineering in Medicine and Biology, Buenos Aires, Argentina, 31 August–4 September 2010*, pp. 3792–3795. New York, NY: IEEE.
38. Wang Q *et al.* 2021 Multi-patient study for coronary vulnerable plaque model comparisons: 2D/3D and fluid–structure interaction simulations. *Biomech. Model. Mechanobiol.* **20**, 1–15. (doi:10.1007/s10237-021-01450-8)
39. Mori H, Torii S, Kutyna M, Sakamoto A, Finn AV, Virmani R. 2018 Coronary artery calcification and its progression: what does it really mean? *JACC: Cardiovasc. Imaging* **11**, 127–142. (doi:10.1016/j.jcmg.2017.10.012)
40. Villiger M *et al.* 2018 Coronary plaque microstructure and composition modify optical polarization: a new endogenous contrast mechanism for optical frequency domain imaging. *JACC: Cardiovasc. Imaging* **11**, 1666–1676. (doi:10.1016/j.jcmg.2017.09.023)
41. Yang C, Bach RG, Zheng J, Naqa IE, Woodard PK, Teng Z, Billiar K, Tang D. 2009 *In vivo* IVUS-based 3-D fluid–structure interaction models with cyclic bending and anisotropic vessel properties for human atherosclerotic coronary plaque mechanical analysis. *IEEE Trans. Biomed. Eng.* **56**, 2420–2428. (doi:10.1109/TBME.2009.2025658)
42. Wang L *et al.* 2017 Effects of residual stress, axial stretch, and circumferential shrinkage on coronary plaque stress and strain calculations: a modeling study using IVUS-based near-idealized geometries. *J. Biomech. Eng.* **139**, 014501. (doi:10.1115/1.4034867)
43. Delfino A, Stergiopulos N, Moore Jr J, Meister J-J. 1997 Residual strain effects on the stress field in a thick wall finite element model of the human carotid bifurcation. *J. Biomech.* **30**, 777–786. (doi:10.1016/S0021-9290(97)00025-0)
44. Schröder J, Brinkhues S. 2014 A novel scheme for the approximation of residual stresses in arterial walls. *Arch. Appl. Mech.* **84**, 881–898. (doi:10.1007/s00419-014-0838-x)